Raman spectroscopy of large extracellular vesicles derived from human microvascular endothelial cells to detect benzo[a]pyrene exposure

Geetika Raizada[1], Benjamin Brunel[1*], Joan Guillouzouic[2], Kelly Aubertin[3], Shinsuke Shigeto[4], Yuka Nishigaki[4], Eric Lesniewska[5], Eric Le Ferrec[2], Wilfrid Boireau[1], Céline Elie-Caille[1]

1. Université de Franche-Comté, CNRS, institut FEMTO-ST ; F-25000 Besançon, France
2. Univ Rennes, Inserm, EHESP, Irset (Institut de Recherche en Santé Environnement et Travail), UMR_S 1085, F-35000, Rennes, France
3. Université Paris Cité, MSC, CNRS, IVETh expertise facility, 45, rue des Saints-Pères, 75006 Paris, France
4. Department of Chemistry, Graduate School of Science and Technology, Kwansei Gakuin University, 1 Gakuen Uegahara, Sanda, Hyogo, 669-1330, Japan
5. ICB UMR 6303 CNRS, University of Bourgogne Franche-Comté, F-21078 Dijon, France

*benjamin.brunel@univ-fcomte.fr

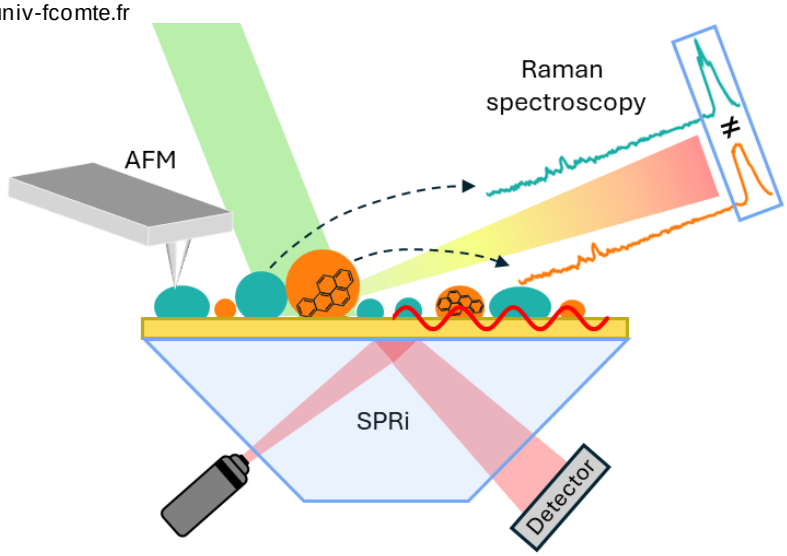

Abstract

Extracellular vesicles (EVs) have shown great potential as biomarkers since they reflect the physio-pathological status of the producing cell. In the context of cytotoxicity, it has been found that exposing cells to toxicants led to changes in protein expression and cargo of the EVs they produce. Here, we studied large Extracellular Vesicles (lEVs) derived from human microvascular endothelial cells (HMEC-1) to detect the modifications induced by cell exposure to benzo[a]pyrene (B[a]P). We used a custom CaF_2-based biochip which allowed hyphenated techniques of investigation: Surface Plasmon Resonance imaging (SPRi) to control the adsorption of objects, atomic force microscopy (AFM) to characterise EVs' size & morphology, and Raman spectroscopy to detect molecular modifications. Results obtained on EVs by Raman microscopy and tip enhanced Raman spectroscopy (TERS) showed significant differences induced by B[a]P in the high wavenumber region of Raman spectra (2800 to 3000 cm^{-1}), corresponding mainly to lipid modifications. Two types of spectra were detected in the control sample. A support vector machine (SVM) model was trained on the pre-processed spectral data to differentiate between EVs from cells exposed or not to B[a]P at the spectrum level; this model could achieve a sensitivity of 88% and a specificity of 99.5%. Whilst 100 % accuracy was achieved at the sample level. Thus, this experimental setup facilitated not only distinguishing between EVs originating from two cell culture conditions but also enabled the discrimination of EV subsets within one cell culture condition.

Keywords Extracellular vesicles, Raman spectroscopy, TERS, AFM, SPRi, machine learning

Introduction

The ever-increasing exposure to different environmental pollutants through various life situations like smoke, diet, water, etc. constitute a rising public health challenge (1). Among these toxicants, polycyclic aromatic hydrocarbons (PAHs) are widely known to increase the cellular oxidative stress (2). This in turns successively generates inflammatory responses because of the influx of reactive oxygen species (ROS) (3) which could lead to DNA damage, lipid peroxidation (4), etc. and ultimately causing cell death. Extracellular vesicles (EVs) have shown a great potential as a biomarker for cytotoxicity (5), as these lipid-membrane enclosed structures are released by different cells and are witnesses, quantitatively and qualitatively, of the physio pathological status of the cells they come from (6). Recently several studies have indicated that chemical pollutants such as PAHs stimulate and alter the release of EVs in the body (7,8). These toxicants also modify the EV composition, especially the molecular cargo (microRNA and proteins), and their uptake alters the cellular function of the host (recipient) cells (9). Previously van Meteren N, et al. studied the role of EVs, especially the small EVs (sEVs) in promoting the oxidative stress induced by PAHs like dibenzo[a,h]anthracene (DBA), benzo[a]pyrene (B[a]P), etc (8). They demonstrated that EVs produced by cells in presence of PAHs contained more iron and their internalisation led to the alteration of mitochondria and lysosomes of the recipient cells. Large EVs (lEVs) are directly or indirectly interlinked with the production and scavenging of ROS, by transferring enzymatic components or signalling molecules that can interfere with cell metabolism, or by being involved in the regulation of redox processes (10). EVs are also known for intercellular transfer of mitochondria, which can also explain the response of EVs associated to cell stress response (11). These evidences strengthen the hypothesis regarding the use of EVs as potential biomarkers of toxicity and in the understanding of the cellular response to PAH exposure (7).

Among different techniques for studying EVs, Raman spectroscopy stands out for its ability to obtain their chemical composition. It is a label-free method through which we can obtain the molecular signature by extracting the spectroscopic information from the vibration of chemical bonds (12). In this spectroscopy, the inelastic scattering of laser light is measured; these photons give the information about the biochemical molecules like proteins, nucleic acids, lipids, etc (13). Its non-contact and non-destructive nature has made it useful for characterization of EVs. Notable applications include the diagnosis of different types of cancer, such as breast cancer (14), prostate cancer (15), (16), or lung cancer (17). It can also be employed for the detection of pathogens, from released EVs (18), as well as for quantifying EV production (19), for example, for therapeutic purposes (20). Several techniques are possible, notably surface-enhanced Raman spectroscopy (SERS) to increase signal intensity, as detailed in two comprehensive reviews on SERS applications to EVs (21), (22). Raman spectroscopy can also be integrated with other methods for multimodal approaches (23), (24) thereby enhancing the depth of information obtained on EVs.

In this study, using Raman spectroscopy, we have characterised lEVs produced by Human microvascular endothelial cell line (HMEC-1) exposed or not to B[a]P. We have developed a new substrate that enabled us to perform several biophysical in situ investigations which includes surface plasmon resonance imaging (SPRi), atomic force microscopy (AFM) and Raman imaging on the same sample. Here, we have illustrated a rigorous method of sample preparation on a gold layered CaF_2 substrate in a controlled way by using SPRi which allows us to control EVs adsorption on the biochip surface and afterwards characterization of the objects on the biochips using AFM for lEVs distribution and Raman investigations. A machine learning model (support vector machine, or SVM) has been applied to perform differentiation of the spectra from the two conditions.

Materials and Methods

1. Cell Culture

Human microvascular endothelial cell line (HMEC-1) obtained from Centre for Disease Control and Prevention (Atlanta, USA) was used for this study. Cells were routinely cultured in petri dishes of 151.9 cm^2 (Corning, Ref

353025) and maintained in endothelial basal medium MCDB131 (US Biological Life Sciences, Ref E3000-01G) adjusted at pH 7.6 with sodium bicarbonate (Gibco, Ref 25080-060) containing 10% decomplemented (56°C, 30min) fetal bovine serum (FBS, Dutscher, Ref 500105A1A), L-glutamine (Gibco, Ref 25030, 10mM final), penicillin/streptomycin (Gibco, Ref 15140-122, 100 unit/mL final), gentamycin (Gibco, Ref 15750-037, 500µg/mL final), epithelial growth factor (EGF, Sigma, Ref E9644, 10ng/mL final) and Hydrocortisone (Up John, Ref 3400932141159, 1µg/mL final). Medium is changed every two to three days. Cells were passed each week by trypsinization (trypsine EDTA 0.05%, Gibco, Ref 25300-054). At 90% confluence, before each treatment, cells were cultured overnight in FBS free medium. Afterwards cells were treated with PAF B[a]P (Benzo[a]pyrene, Sigma, Ref B1760), which was prepared as a stock solution in dimethyl sulfoxide (DMSO, Sigma, Ref D8418). Final vesicle concentration did not exceed 0.0005% (v/v) and control cultures received the same volume of DMSO.

2. Isolation of EV from HMEC-1 cells

As previously reported in Le Goff et al. (7), conducted according to the international guidelines for extracellular isolation (MISEV 2023), the serum free conditioned media was first centrifuged at 3650 x g for 10 min at 4°C to remove entire cells and cell debris. The clarified supernatant was collected and ultracentrifuged at 10 000 x g for 30 min at 4°C (Optima L-90 K ultracentrifuge and Sw 28.1 Ti rotor or XE-90 ultracentrifuge and Sw 32 Ti rotor), Beckman Coulter, USA). The EV pellet obtained is re-centrifuged in PBS 1X (Gibco, 14190-094) for a washing step (10 000 x g for 30 min at 4°C). The final EV pellet was suspended in 50 µl PBS 1X and stored at -20°C. The EVs concentration was measured by Nanoparticle Tracking Analysis, (NanoSight NS300, Malvern Instruments, UK) with a protocol of 5*60s videos.

3. Substrate/SPRi

MATLAB simulation was performed to generate and predict the plasmon response of the new substrate material calcium fluoride (CaF_2) which emits negligible Raman scattering light (minimal baseline with a single sharp peak at 320 cm^{-1}). The program written by Luigi Cristofolini (2022) (25) was modified according to our system, as we used a gold biochip instead of a gold covered prism. The refractive index for CaF_2 and gold was taken as 1.43 & 0.16 respectively; the adsorption coefficient for gold was determined to be 3.889 by simulating the plasmon response on glass (SF11) by leveraging the information from the previous experiments.

These biochips were composed of 12.5 mm by 28 mm CaF_2 slides (custom order from *Crystran, Ltd*. U.K.) covered with a thin gold layer (~40 nm) that has an adhesive layer of titanium Ti (~ 3nm) in between; and were manufactured using Plassys DC magnetron sputtering in the *MIMENTO* clean room facilities of the FEMTO-ST Institute (Besançon, France) (26).

The gold biochips were cleaned with ethanol, milli-Q water and dried under nitrogen. Then the cleaned gold biochip was mounted in the Surface Plasmon Resonance imaging (Horiba SPRi-Plex II) system. Several regions of interest (ROI) of 500 µm in diameter were defined across the biochip surface to optimally monitor the EV adsorption. After obtaining plasmon curves, the sample was injected using a microfluidic system, the flow rate of the running buffer (PBS, Sigma, P4417) was set to 10 µl/min and the sensorgram was monitored during the 20 min sample injection (EV concentrations ~ 10^8 EVs/ml). As the sample gets physisorbed on the surface of the biochip, we noticed a change in the reflectivity variation (%). The biochip was then washed gently inside the SPRi system with milli-Q water (to avoid salt crystallisation on the surface); the biochips were subsequently gently dried to be characterised under AFM and then Raman confocal microscope (24).

4. AFM

AFM imaging was performed using the *Bruker Nanowizard®4 Bioscience* system. For the imaging, the triangular Pyrex-Nitride AFM tips (obtained from *NanoAndMore*) with spring constant 0.08 N/m were used in tapping mode (AC mode) in air. The scanning was done in randomly selected different areas across the biochip, all the images

obtained were of the same size 2x2 μm^2 with the resolution of 512 x 512 pixels at the line rate 1.0 Hz. The value of setpoint and drive amplitude was first determined after calibrating the tip and then the values were further optimised according to the quality of the image obtained. The images were treated using *Mountain's SPIP 9* software to obtain the size profile and EV density on the biochip surface. We used particle analysis to detect and count the EVs present; and in order to selectively include only EVs, we used a threshold by height and kept it at 8.5 nm. Lastly any particle with a very small area (smaller than 10^{-5} μm^2) was eliminated.

5. Raman microscopy

a. Acquisition

After AFM characterization, the biochips were characterized by Raman microscopy. Raman spectra were acquired using a DXR3xi Raman imaging microscope (Thermo Fisher Scientific), equipped with a 50x objective and setting the confocal pinhole to 50 µm. Samples were illuminated with a 532 nm laser with a power of 10 mW (maximal laser power). Camera exposure was set to 200 ms, with 50 accumulations. ROIs were selected at different places of the biochip, based on the amount of material visible in brightfield view and the intensity of Raman signal tested with a short acquisition of 2 s (live detection mode). Spectra were mapped over the ROI, with a spatial step of 3 µm, and Raman shifts ranging from 50 cm^{-1} to 3400 cm^{-1}.

b. Data pre-processing

All data processing was performed using the Python programming language. Raw spectra were first truncated to keep only Raman shifts above 400 cm^{-1}. Then, for each spectrum, the baseline was subtracted using the arPLS method (27). The intensity corresponding to Raman shift below 450 cm^{-1} were then truncated as the baseline correction can cause unwanted edge effects. Spectra were subsequently normalised, setting the average intensity in the high wavenumber (HWN) lipid band (2835 cm^{-1} to 2970 cm^{-1}) to 1 and the average intensity in the bio-silent region (1900 cm^{-1} to 2500 cm^{-1}) to 0.

Spectra with insufficient quality were then removed as follows. First, spectra with a signal-to-noise ratio (SNR) below 10 were removed (10,019 spectra out of 10,830). SNR was calculated as the ratio between the average intensity in the HWN region and the standard variation in the bio-silent region. Secondly, spectra showing that the sample was locally burned by the laser were removed (118 out of 811). Those pixels were identified by comparison with the spectrum of a voluntary burnt area, quantified as the dot product between the two spectra in range 1130 cm^{-1} to 1700 cm^{-1} (D and G bands of graphene spectrum). Spectra with a dot product over 800 a.u. were removed (threshold determined empirically by visual observation of the spectra).

6. Tip enhanced Raman spectroscopy (TERS)

The classical SPRi biochip consisting of glass (SF11) and gold layer (50 nm) was used for preparing the sample of TERS experiments. The preparation of these biochips with EV samples using SPRi was the same as we have described previously. Samples were taken from the same batches as those used for microscopy.

a. Acquisition

TERS spectra were acquired using an AFM–Raman integrated system (XploRA Nano, Horiba). Au-coated TERS-active AFM probes made of Si (OMNI TERS-NC-Au-5, AppNano) were used to obtain AFM images and TERS spectra of single EVs. The probe had a resonant frequency of 300 kHz and dimensions of 150 x 50 x 5.4 μm^3. Samples were illuminated from the side with a 638 nm laser with a power of 0.65 mW. Camera exposure was set to 5 s, with 1 accumulation, repeated 5 times. First, AFM images were taken in tapping mode (see supplementary information, Fig. S1 and S2), and then TERS spectra were measured from single EVs, with Raman shifts ranging from 150 cm^{-1} to 3760 cm^{-1}. Spectra of 6 EVs derived from cells exposed to B[a]P and of 3 EVs of the control sample were acquired, with diameters ranging from 71 to 283 nm.

b. Data pre-processing

The far-field Raman signal (without the TERS probe) was subtracted from the spectra measured with the TERS probe approached. The resulting TERS spectra were then truncated to keep only the HWN region (2800 cm^{-1} to 3050 cm^{-1}). Spectra were subsequently normalised, setting the average intensity in the 2835 cm^{-1} to 2970 cm^{-1} range to 1 (same as for Raman microscopy) and the average intensity between 3050 cm^{-1} and 2975 cm^{-1} to 0.

Due to the high intensity of the local electric field (SERS), the samples were burned, locally adding a Raman signature of amorphous carbon, especially in the fingerprint region. For each EV, 5 spectra were taken. The spectra showing a sample that was too burned or presenting a "forest" of peaks due to the reaction were excluded before averaging by EV.

7. Statistical analysis

Statistical analysis was performed using scikit-learn Python package. Once the spectra had been pre-processed, the principal component analysis (PCA) method was used, both to study spectral variation and to reduce the number of variables. PCA allows data to be projected onto one or more perpendicular axes (principal components) along which variability is greatest.

A supervised machine learning model was then used to assess the possibility of distinguishing between the spectra coming from control and treated EVs. The support vector machine (SVM) model was chosen as it is a classical model that can be non-linear thanks to a kernel (here, radial basis function). The model's capabilities were assessed by a leave-one-out validation, leaving out one pixel, one sample or one EV as appropriate (detailed below).

Results & Discussion

1) SPRi and Raman spectroscopy compatible substrate

In our previous works, SPRi substrates were made from SF11 glass. However, SF11 gives a non-negligible signal in Raman spectroscopy. For this reason, we replaced it with CaF_2 which is commonly used in Raman spectroscopy as it does not emit Raman scattering light in the range studied [24]. To test whether CaF_2 substrates would still be compatible with SPRi, i.e., if the change in refractive index would not impair the excitation of plasmons, we carried out simulations, as detailed in Fig. 1. In Fig. 1a we can observe the calculated plasmon curve for SF11 with gold layer of 50 nm in thickness; we chose the values of gold refractive index along with its absorption coefficient to obtain a theoretical data as close as possible to the experimental data shown in Fig. 1c. Once, the parameters were fixed, we simulated the plasmon response of CaF_2 slide. Although some fluctuations were obtained in the case of CaF_2 as can be observed in Fig. 1b which might be due to the change in refractive index from prism to the substrate, the general trend was the same in both simulations, with a plasmon excitation at an angle around 59°. This suggested that CaF_2 substrate were still compatible with SPRi. We then checked this result experimentally with our SPRi apparatus, by measuring the same plasmon curve for CaF_2 Fig. 1d. The results obtained from SPRi experiment yielded the same conclusion as that of simulation; despite having the sensitivity of 62 %/°, as compared to 90 %/° with SF11, (Fig. 1f) the plasmon response surpassed the limit of detection, having no discernible influence on kinetics monitoring during the sample injection. In conclusion, the use of CaF_2 made our biochip compatible with Raman spectroscopy, while remaining compatible with the optical set-up of the SPRi instrumentation.

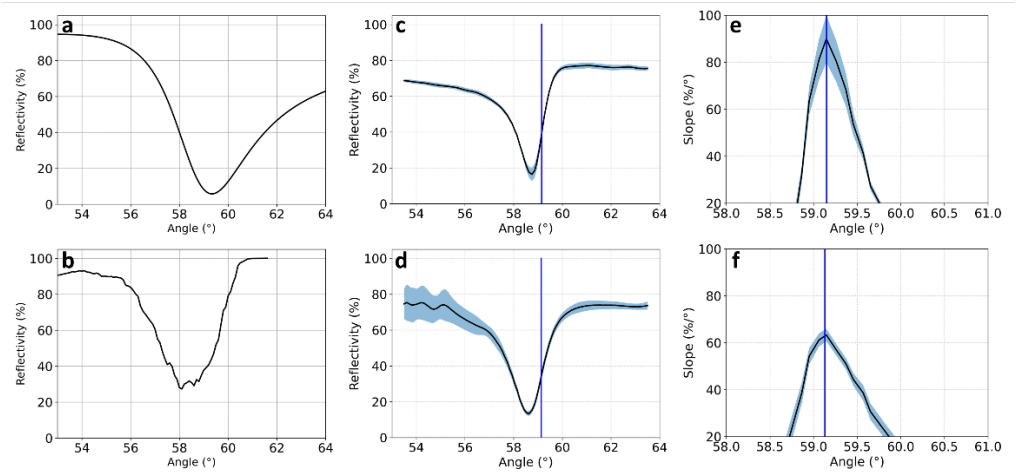

Fig. 1 Plasmon curves of the gold biochips obtained in water: a) Simulated plasmon curve of SF11 substrate with a 50 nm gold layer ; b) Simulated plasmon curve of CaF_2 substrate with a 40 nm gold layer ; c) Experimental plasmon curve obtained for SF11 ; d) Experimental plasmon curve for CaF_2 ; e) Slope curve of SF11 ; f) Slope curve of CaF_2 substrate. Note: the vertical blue line in c,d,e and f represents the chosen working angle for further SPRi measurements. The shaded areas correspond to the standard deviation calculated on all ROIs.

2) Kinetic monitoring of EV deposition by SPRi

The new biochip was used to monitor the adsorption of EVs using SPRi system which allowed a complete control over the flow rate and the interaction time between the sample and biochip surface. We injected sample at 10 µl/min for 20 mins to provide ample time for the sample to adsorb on the surface. Different regions of interest were defined in the sensitive window of the biochip surface where R1, R2 and so on represents the spots in the same row (Fig. 2e). In the Fig. 2a & c, we can observe the gradual increase in the reflectivity over the duration of the sample injection which indicates the deposition of biomaterials on the biochip. The difference in the reflectivity variation at different rows of ROI was due to the mass transfer that occurs all along the path of the sample under flow, and which created a gradient of objects adsorbed. We measured the reflectivity variation between the start of the injection and ten minutes after the end of injection (Fig. 2a & c) are the examples of experiment done with EV control and treated sample). The average response obtained for the control sample and treated sample on all ROIs were 1.9 ± 0.4 and 2.9 ± 0.4 respectively (Fig. 2f). With the SPRi experiments, we ensured the reproducibility in the preparing the samples, the quantity of material absorbed, for the Raman imaging experiments.

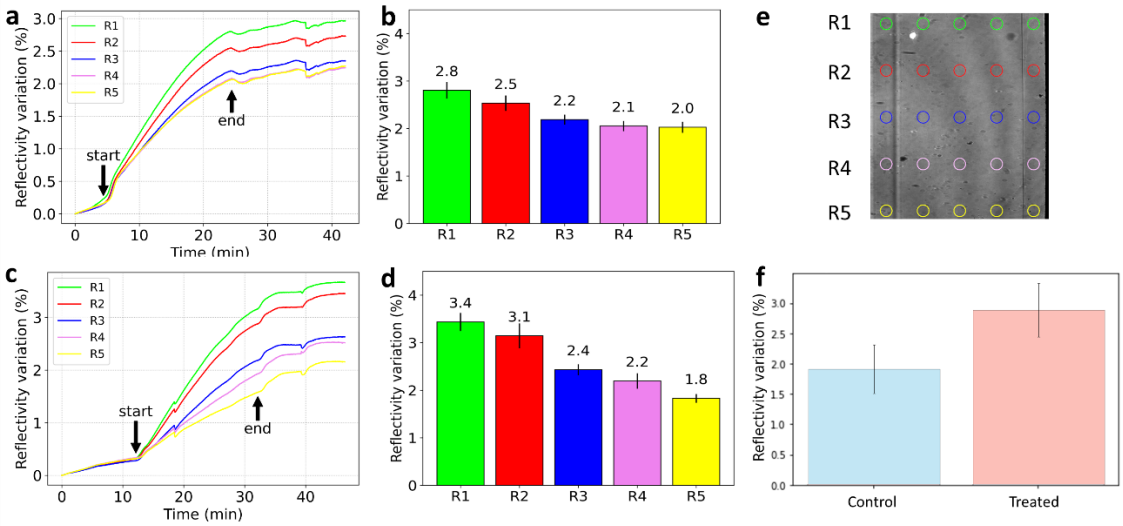

Fig. 2 Sensorgrams and response (reflectivity variation) obtained during EV adsorption on biochips: kinetic monitoring of (a) control sample injection and (c) treated sample, reflectivity variation after 10 mins of the (b) control and (d) treated sample injection. e) The average response obtained for the triplicate experiments with each sample; with error bar indicating the deviation between the experiments. f) Picture of the biochip with circles indicating the ROIs organized in 5 lines: from R1 near the flow arrival to R5.

3) Characterization and size distribution by AFM

After preparing the biochips covered with EVs, we characterised them with the help of AFM (Fig. 3a,e). AFM scanning was done to obtain the surface coverage, metrology and morphology of the EVs that were adsorbed. The AFM scanning was performed in the identical area as the regions R1 and R2 defined in the SPRi experiment. The characterization with AFM allowed us to obtain the size profile of adsorbed objects, in terms of height, diameter, and projected area. Through *Mountain's SPIP's particle analysis,* we counted 1485 particles for control and 1349 particles for treated condition, which provided us statistically reliable and relevant results. The particle density (surface coverage) was around $5.7 \pm 0.7 \times 10^6$ particles/mm^2 for the control condition and $4.2 \pm 0.3 \times 10^6$ particles/mm^2 for the treated condition. We also measured the diameter; in this case, we chose the maximum diameter, which is taken from the centre of gravity of the particle. For both conditions, approximately 70 % of the particles counted had maximum diameter lower than 200 nm, which is consistent with the NTA data where the largest peak obtained at 180 nm (see supplementary information, Fig. S3). Fig. 3i shows the size distribution of the objects that were adsorbed on our biochips. We observed that there are different large EV subpopulations present in both samples which ranged from 200 nm in size to 1600 nm. In the biochip, the presence of some aggregates of lEVs were evident, as depicted in Fig. 3b. Also, these lEVs exhibited the height spanning from 40 nm to 100 nm, as illustrated in Fig. 3d & h. This observation sheds light on the diversity and organization of EVs within the experimental setup. It is of interest to note that EVs coming from the treated condition contained to have slightly bigger diameter subpopulation than the control sample (Fig. 3j); the average of maximum diameter was 352 ± 159nm for control condition and 392 ± 232 nm for treated condition. In 2022, Sbarigia C. et al. (28) have also remarked that the microvesicles (MVs) derived from H_2O_2 treated cells had a wider diameter than the MVs from the control cells. The larger diameter of EVs from treated condition might explain the higher response obtained in SPRi experiment.

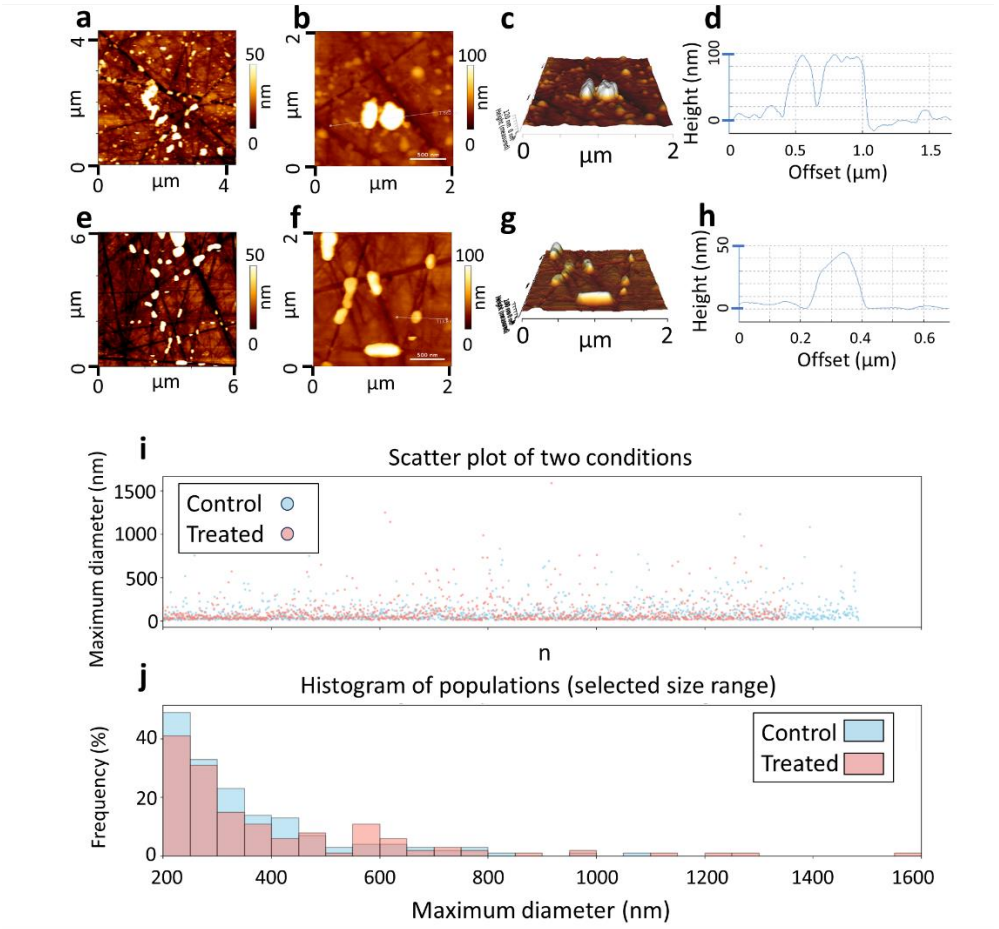

Fig. 3 AFM characterization: large-area images representing measured heights (a, e) and subsequent close-ups (b, f), with the corresponding 3D generated images (c, g) and section profiles (d, h), to obtain the morphology and size of EVs from control (a, b, c, d) and treated (e, f, g, h) conditions. Scatter plot of the particles measured by AFM (n: number of particles counted) & size distribution of lEVs for both conditions.

4) Differences in EV sub-populations induced by B[a]P

AFM was used to verify the presence of lEVS adsorbed on the surface of our biochip, and to characterize them morphologically. We then used Raman spectroscopy to further characterize the lEVs and identify the potential biochemical modifications induced by B[a]P exposure.

As shown in Fig. 4a, spectra showed a stronger signal in the HWN region (from 2800 cm^{-1} to 3100 cm^{-1}) than in the fingerprint region (from 450 cm^{-1} to 1900 cm^{-1}). HWN bands correspond to vibrations of carbon-hydrogen bonds, which are mainly present in lipids: 2932 cm^{-1} for $\nu_s(CH_3)$, 2882 cm^{-1} for $\nu_{as}(CH_2)$ and 2853 cm^{-1} for $\nu_s(CH_2)$. In the fingerprint region, peaks corresponding to proteins and lipids were found: 1665 cm^{-1} for amide I band (peptide bond), 1602 cm^{-1} for tyrosine and tryptophan, 1446 cm^{-1} for CH_2 and CH_3 bending, 1302 for CH_2 twisting and 1003 cm^{-1} for the phenylalanine residue of proteins. Higher noise in the fingerprint region prevented the identification of additional vibrations.

The peaks identified are consistent with EV spectra found in the literature. The lipid signature is always present, with peaks at 1446 cm^{-1} and between 2800 and 3000 cm^{-1} generally being the most intense (14,16,19,29), although the HWN region is rarely measured. A protein signature is also frequently observed jointly, with the Amide I peak (1665 cm^{-1}) and phenylalanine peak (1003 cm^{-1}) being the most readily identified (16,19,29). Finally,

some publications identify nucleic bases giving specific peaks between 720 and 800 cm^{-1} (20,30). These peaks are generally less intense than the previous ones and have not been detected here.

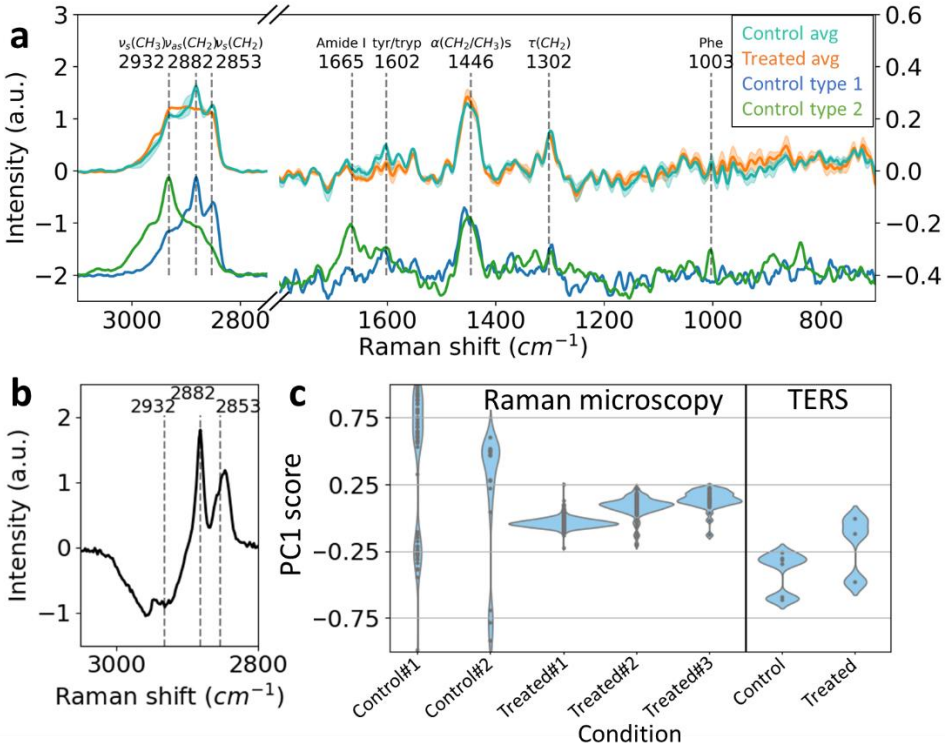

Fig. 4 (a) Average and standard deviation (shades) of Raman spectra of EVs from control and treated condition (top). Single pixel spectra representative of the 2 different types of control spectra found in the dataset (bottom). PCA results, with PC1 (b) and scores (c) for each sample in Raman microscopy and TERS. The dots correspond to pixels in the Raman microscopy (n = 59, 16, 463, 119 and 36 from left to right) section and to single EVs (n=6 and 3) in the TERS section.

While spectra from EVs in treated conditions were rather homogeneous, two types of spectra were observed in control condition (Fig. 4a, bottom). To quantify each population in the different samples (treated, control type 1 and control type 2), we applied principal component analysis (PCA). PCA was used to represent the spectra on the axis with the greatest variance (first principal component, Fig. 4b). The method was only applied to the HWN region because it had a better SNR and a clear variation between the three types of spectra. Fig. 4c shows the violin plot of PC1 score of each spectrum for each sample of both control (DMSO) and treated (B[a]P) conditions. PC1 scores reflect how close the spectra are from the spectra in Fig. 4a: -1 corresponds to "Control type 2", 0 correspond to "Treated" and 1 corresponds to "Control type 1". The number of spectra for each sample (Control#1, Control#2, Treated#1, Treated#2, Treated#3) were 59, 16, 463, 119 and 36 respectively. Similar distributions were found from a batch to another, with clear differences between the two conditions.

Spectra from control conditions presented 2 types of spectra, likely corresponding to two sub-populations of EVs, either close to type 1 or type 2. Type 1 displayed peaks corresponding to lipids (2932, 2882, 2853, 1446 and 2302 cm^{-1}), most probably coming from EV membrane. The ratios between peaks 2932, 2882 and 2853 cm^{-1} correspond to saturated fatty acids with a carbon chain of 14 to 20 carbons, as observed elsewhere (31). However, it is difficult to tell the type of lipid (phospholipids (PC, PS, PE), sphingomyelin, …) because the Raman signature of lipids comes essentially from fatty acids, especially in the HWN region. Type 2 displayed peaks

corresponding to proteins (1655, 1602 and 1003 cm^{-1})(32), and represented 26±8 % of the spectra. This could correspond to a cargo present in some EVs, notably mitochondria, as their Raman spectrum resembles type 2 (33) and we know that these EVs can contain it (34). Type 1 would then correspond to a population of EV without a mitochondrion. A cargo could still be present, but with a Raman signal masked by the one coming from the lipids of the membrane.

Spectra from treated condition presented a single population with a spectrum being roughly the average of Control type 1 and 2. One explanation could be that B[a]P exposure drives EV production towards a given population which is otherwise heterogeneous. It could be that the presence of a new cargo masks the difference in Raman signal between the two populations. The HWN signal of treated EVs could be close to that of free cholesterol (31), but this would need to be confirmed, notably with additional fingerprint measurements.

We note that the treated EVs spectrum does not correspond to the spectrum of B[a]P molecule itself (35) or its metabolites. The change in spectrum due to B[a]P is thus probably due to a change in the biogenesis and/or phenotype of EVs (8), rather than a minor changes in the components themselves (lipid peroxidation, protein carbonyls) (36) or a residue of B[a]P in the conditioned medium.

From Fig. 4c, it seems that PC1 scores allow discrimination between each population. We tested this idea by training and testing a SVM supervised classifier with a radial basis function kernel. The model was tested using a leave-one out cross validation (LOOCV) algorithm, i.e. it was trained on all spectra but one and tested on that remaining spectrum, repeating the process for each spectrum to get a prediction for all spectra. Resulting predictions are presented in the confusion matrix in Fig. 5a. To balance the number of samples of each condition, copies of the minority class were added in the training dataset.

The same process was tested at the sample level rather than the spectrum level. For each sample, a prediction of each of its spectrum was made, as described above, then the class of the sample was deduced as the majority class of its spectra. The model was again tested with a LOOCV, but at the sample level. The resulting predictions are presented in Fig. 5c.

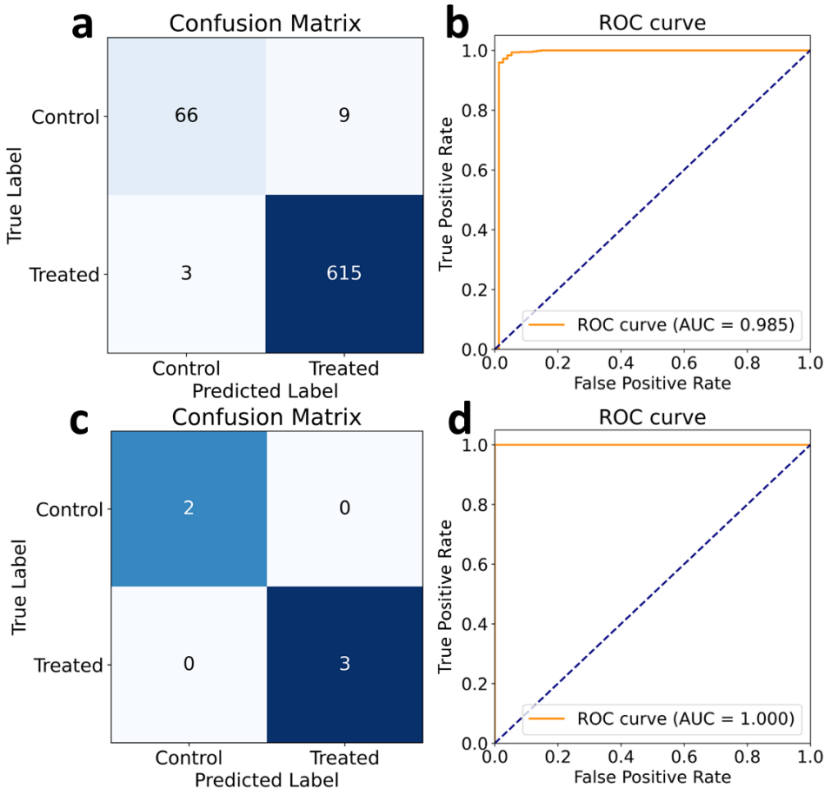

Fig. 5 Confusion matrix and ROC curve of the classifier predictions at the spectrum level (a, b) (leave one spectrum/pixel out validation) and at the sample level (d, e) (leave one sample out validation, predictions based on majority vote from sample spectra).

At the spectrum level, the model achieved a sensitivity of 88.0% and a specificity of 99.5%, with an area under the curve (AUC) in the Receiver Operating Characteristic (ROC) curve of 0.985. This indicates a reproducible and clear distinction between spectra of EVs derived from cells exposed to DMSO (control) or B[a]P. At the sample level, the model gives a 100% accurate prediction. Even if few spectra are misclassified, the majority class is still correct. Thus, our model is capable of classifying EVs obtained from HMEC-1 cells, distinguishing whether the cells were exposed to B[a]P or not (control) through Raman microscopy.

5) Raman spectroscopy at the single EV scale: TERS

In order to confirm whether the previous spectra were indeed coming from EVs, TERS experiments were conducted on similar samples, but at the single EV level. TERS allowed us to simultaneously measure the diameters and the Raman spectra of EVs. From the AFM images obtained with the TERS system, we selected EVs with diameters between 71 and 283 nm for Raman measurement. Note that for Raman spectroscopy, measurements were also close to single EV measurements as the average number of EV per focal spot (~0.5 μm^2) was in the order of few EVs.

Fig. 6 shows the average (solid line) and the standard deviation (shades) of spectra of EVs from control (green, n = 6 EVs) and treated (orange, n = 3 EVs) samples. Similar to bulk Raman microscopy, only the HWN signal presented a sufficiently intense signal to be exploited.

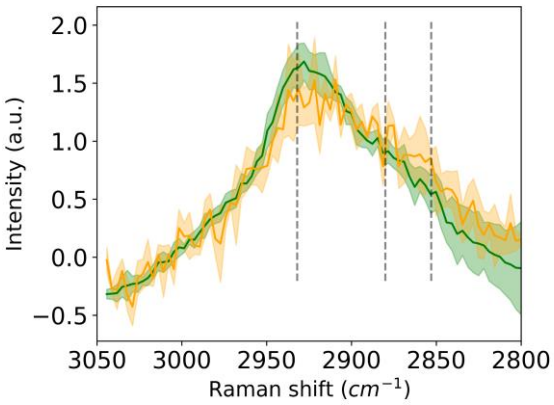

Fig. 6 TERS spectra of EVs derived from cells exposed to B[a]P (orange, n = 3) or control (green, n= 6).

The SNR is not as good as with bulk Raman microscopy, but significant differences were also found at 2932 cm^{-1} and 2853 cm^{-1}. The reduced spectral resolution prevented the acquisition of sharp peaks as for bulk microscopy. Supervised classification models developed for analysing bulk Raman microscopy data were applied to TERS results. Fig. 4c shows the PC1 scores in TERS samples. We compared the PC1 score of each EV with its size. PC1 scores were found to be inversely correlated to diameters, with a correlation coefficient of -0.64. This could explain why no spectra close to Control type 1 (PC1 score close to 1) were measured, as we tried to select bigger EVs in TERS. The correlation is also consistent with spectrum Control type 2 corresponding to mitochondria: the bigger the EV the more fragments of broken mitochondria it can contain.

Overall, results similar to Raman microscopy were found, with B[a]P treated EV in the -0.25/0.25 range (except one) and control EV outside this range (Fig. 4c). The SVM classifier model was also applied after being trained on Raman microscopy PC1 scores. As shown in the confusion matrix (Fig. 7), a sensitivity of 66.7 % and a specificity = 100.0 % were obtained, with an AUC of the ROC curve of 0.72. This means that our model is capable of classifying EVs derived from cells that were exposed to B[a]P or not (control), at the single EV level through TERS.

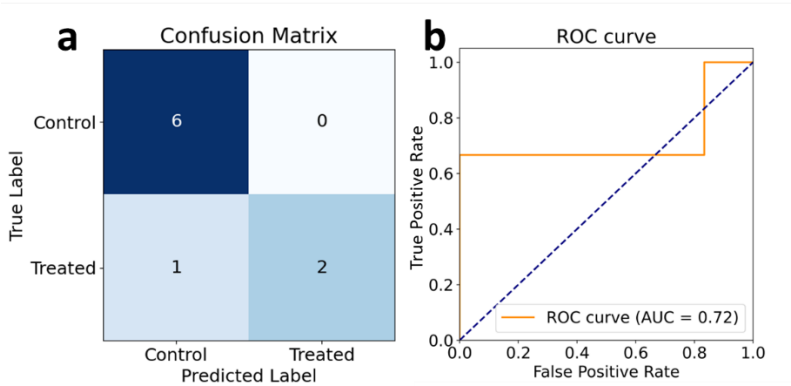

Fig. 7 Confusion matrix (a) ROC curve (b) of the classifier predictions of TERS spectra of EVs adsorbed on chip from control and B[a]P treated conditions (leave one spectrum/EV out validation).

Conclusion

In this study, we aimed to investigate the impact of HMEC cell treatment with B[a]P on the molecular signatures of EVs produced. We introduced a comprehensive methodology, from controlled sample preparation to obtaining molecular signature, by combining different techniques like SPRi, AFM and Raman spectroscopy.

Through AFM studies, we recognized that there were several EV subpopulations present according to their size distribution. We also observed that the treatment with B[a]P, led the cells to produce slightly larger sized EVs than from control cell conditions. The investigation with Raman spectroscopy revealed two different types of spectra for EVs from control condition and one kind of spectra from the treated condition, differences corresponding mainly to lipid modifications. The utilization of SVM model aided in the discrimination of spectra coming from the two conditions, with a sensitivity of 88% and a specificity of 99.5%. In conclusion, our method highlighted the differences brought due to cytotoxic conditions. The high specificity and sensitivity of this method have shown a potential to be used for diagnostic applications.

Acknowledgments & funding

We thank the iVETh platform for allowing us to use their Raman microscopy system and particularly Fabien Picot for the training and the assistance during data acquisition. S.S. is grateful to Dr. Shinsuke Kashiwagi (HORIBA, Japan) for initiating the collaboration between the French and Japanese groups and for supporting the TERS experiment. IVETh is supported by the IdEx Université Paris Cité, ANR-18-IDEX-0001, by the Region Ile de France under the convention SESAME 2019 – IVETh (EX047011) and via the DIM BioConvS, by the Region Ile de France and Banque pour l'Investissement (BPI) under the convention Accompagnement et transformation des filières projet de recherche et développement N° DOS0154423/00 & DOS0154424/00, DOS0154426/00 & DOS0154427/00 , and Agence Nationale de la Recherche through the program France 2030 "Integrateur biotherapie-bioproduction" (ANR-22-AIBB-0002). This work has been supported by the EIPHI Graduate School (contract ANR-17-EURE-0002) and Bourgogne-Franche-Comté Region. This work was supported by the French National Agency for Research (ANR; ENDOMITOPAH project: R23137NN). This work was partly supported by the French RENATECH network and its FEMTO-ST technological facility. Authors would like to acknowledge support of the CNRS/UFC CLIPP platform in the SPRi characterization of EVs.

Authors' contributions

All authors contributed to the study conception and design. Material preparation was performed by J. Guillouzouic, E. Le Ferrec and G. Raizada. Data collection was conducted by G. Raizada, B. Brunel and Y. Nishigaki. Data analysis was performed by G. Raizada, and B. Brunel. The work was supervised by C. Elie-Caille, W. Boireau, E. Le Ferrec, E. Lesniewska, S. Shigeto and K. Aubertin. The first draft of the manuscript was written by G. Raizada and B. Brunel and all authors commented on previous versions of the manuscript. All authors read and approved the final manuscript.

Data availability

The pre-processed Raman spectra dataset generated and analyzed during the current study is available in the dat@UBFC repository (http://dx.doi.org/doi:10.25666/DATAUBFC-2024-07-19).

Conflict of interest

The authors declare that they have no conflict of interest.

References

1. Starski A, Kukielska A, Postupolski J. Occurrence of polycyclic aromatic hydrocarbons in human diet - exposure and risk assessment to consumer health. Rocz Panstw Zakl Hig. 2021;72(3):253-65.

2. Hoffman JB, Petriello MC, Hennig B. Impact of nutrition on pollutant toxicity: an update with new insights into epigenetic regulation. Rev Environ Health. 1 mars 2017;32(1-2):65-72.

3. Schlezinger JJ, Struntz WDJ, Goldstone JV, Stegeman JJ. Uncoupling of cytochrome P450 1A and stimulation of reactive oxygen species production by co-planar polychlorinated biphenyl congeners. Aquat Toxicol. 25 mai 2006;77(4):422-32.

4. Deng Q, Dai X, Guo H, Huang S, Kuang D, Feng J, et al. Polycyclic Aromatic Hydrocarbons-Associated MicroRNAs and Their Interactions with the Environment: Influences on Oxidative DNA Damage and Lipid Peroxidation in Coke Oven Workers. Environ Sci Technol. 1 avr 2014;48(7):4120-8.

5. Carberry CK, Rager JE. The impact of environmental contaminants on extracellular vesicles and their key molecular regulators: A literature and database-driven review. Environ Mol Mutagen. 2023;64(1):50-66.

6. Simons M, Raposo G. Exosomes – vesicular carriers for intercellular communication. Curr Opin Cell Biol. 1 août 2009;21(4):575-81.

7. Le Goff M, Lagadic-Gossmann D, Latour R, Podechard N, Grova N, Gauffre F, et al. PAHs increase the production of extracellular vesicles both in vitro in endothelial cells and in vivo in urines from rats. Environ Pollut. 1 déc 2019;255:113171.

8. van Meteren N, Lagadic-Gossmann D, Chevanne M, Gallais I, Gobart D, Burel A, et al. Polycyclic Aromatic Hydrocarbons Can Trigger Hepatocyte Release of Extracellular Vesicles by Various Mechanisms of Action Depending on Their Affinity for the Aryl Hydrocarbon Receptor. Toxicol Sci. 1 oct 2019;171(2):443-62.

9. Eckhardt CM, Baccarelli AA, Wu H. Environmental Exposures and Extracellular Vesicles: Indicators of Systemic Effects and Human Disease. Curr Environ Health Rep. 1 sept 2022;9(3):465-76.

10. Bodega G, Alique M, Puebla L, Carracedo J, Ramírez RM. Microvesicles: ROS scavengers and ROS producers. J Extracell Vesicles. 1 déc 2019;8(1):1626654.

11. Liu D, Dong Z, Wang J, Tao Y, Sun X, Yao X. The existence and function of mitochondrial component in extracellular vesicles. Mitochondrion. 1 sept 2020;54:122-7.

12. Zhang P, Wang L, Fang Y, Zheng D, Lin T, Wang H. Label-Free Exosomal Detection and Classification in Rapid Discriminating Different Cancer Types Based on Specific Raman Phenotypes and Multivariate Statistical Analysis. Molecules. janv 2019;24(16):2947.

13. Zhang H, Silva AC, Zhang W, Rutigliano H, Zhou A. Raman Spectroscopy characterization extracellular vesicles from bovine placenta and peripheral blood mononuclear cells. PLOS ONE. 2 juill 2020;15(7):e0235214.

14. Penders J, Nagelkerke A, Cunnane EM, Pedersen SV, Pence IJ, Coombes RC, et al. Single Particle Automated Raman Trapping Analysis of Breast Cancer Cell-Derived Extracellular Vesicles as Cancer Biomarkers. ACS Nano. 4 nov 2021;

15. Lee W, Nanou A, Rikkert L, Coumans FAW, Otto C, Terstappen LWMM, et al. Label-Free Prostate Cancer Detection by Characterization of Extracellular Vesicles Using Raman Spectroscopy. Anal Chem. 2 oct 2018;90(19):11290-6.

16. Lee W, Lenferink ATM, Otto C, Offerhaus HL. Classifying Raman spectra of extracellular vesicles based on convolutional neural networks for prostate cancer detection. J Raman Spectrosc. 2020;51(2):293-300.

17. Shin H, Jeong H, Park J, Hong S, Choi Y. Correlation between Cancerous Exosomes and Protein Markers Based on Surface-Enhanced Raman Spectroscopy (SERS) and Principal Component Analysis (PCA). ACS Sens. 28 déc 2018;3(12):2637-43.

18. Qin YF, Lu XY, Shi Z, Huang QS, Wang X, Ren B, et al. Deep Learning-Enabled Raman Spectroscopic Identification of Pathogen-Derived Extracellular Vesicles and the Biogenesis Process. Anal Chem. 13 sept 2022;94(36):12416-26.

19. Zini J, Saari H, Ciana P, Viitala T, Lõhmus A, Saarinen J, et al. Infrared and Raman spectroscopy for purity assessment of extracellular vesicles. Eur J Pharm Sci Off J Eur Fed Pharm Sci. 1 mai 2022;172:106135.

20. Gualerzi A, Kooijmans SAA, Niada S, Picciolini S, Brini AT, Camussi G, et al. Raman spectroscopy as a quick tool to assess purity of extracellular vesicle preparations and predict their functionality. J Extracell Vesicles. 2019;8(1):1568780.

21. Shin H, Seo D, Choi Y. Extracellular Vesicle Identification Using Label-Free Surface-Enhanced Raman Spectroscopy: Detection and Signal Analysis Strategies. Mol Basel Switz. 9 nov 2020;25(21):E5209.

22. Guerrini L, Garcia-Rico E, O'Loghlen A, Giannini V, Alvarez-Puebla RA. Surface-Enhanced Raman Scattering (SERS) Spectroscopy for Sensing and Characterization of Exosomes in Cancer Diagnosis. Cancers. janv 2021;13(9):2179.

23. Beekman P, Enciso-Martinez A, Rho HS, Pujari SP, Lenferink A, Zuilhof H, et al. Immuno-capture of extracellular vesicles for individual multi-modal characterization using AFM, SEM and Raman spectroscopy. Lab Chip. 23 juill 2019;19(15):2526-36.

24. Raizada G, Namasivayam B, Obeid S, Brunel B, Boireau W, Lesniewska E, et al. Multimodal Analytical Platform on a Multiplexed Surface Plasmon Resonance Imaging Chip for the Analysis of Extracellular Vesicle Subsets. JoVE J Vis Exp. 17 mars 2023;(193):e64210.

25. Cristofolini L. Surface Plasmon Resonance Calculator [Internet]. Disponible sur: https://www.mathworks.com/matlabcentral/fileexchange/13700-surface-plasmon-resonance-calculator

26. Remy-Martin F, El Osta M, Lucchi G, Zeggari R, Leblois T, Bellon S, et al. Surface plasmon resonance imaging in arrays coupled with mass spectrometry (SUPRA–MS): proof of concept of on-chip characterization of a potential breast cancer marker in human plasma. Anal Bioanal Chem. 1 août 2012;404(2):423-32.

27. Baek SJ, Park A, Ahn YJ, Choo J. Baseline correction using asymmetrically reweighted penalized least squares smoothing. Analyst. 1 déc 2014;140(1):250-7.

28. Sbarigia C, Tacconi S, Mura F, Rossi M, Dinarelli S, Dini L. High-resolution atomic force microscopy as a tool for topographical mapping of surface budding. Front Cell Dev Biol. 2022;10:975919.

29. Kruglik SG, Royo F, Guigner JM, Palomo L, Seksek O, Turpin PY, et al. Raman tweezers microspectroscopy of circa 100 nm extracellular vesicles. Nanoscale. 23 janv 2019;11(4):1661-79.

30. Chalapathi D, Padmanabhan S, Manjithaya R, Narayana C. Surface-Enhanced Raman Spectroscopy as a Tool for Distinguishing Extracellular Vesicles under Autophagic Conditions: A Marker for Disease Diagnostics. J Phys Chem B. 3 déc 2020;124(48):10952-60.

31. Czamara K, Majzner K, Pacia MZ, Kochan K, Kaczor A, Baranska M. Raman spectroscopy of lipids: a review. J Raman Spectrosc. 2015;46(1):4-20.

32. Rygula A, Majzner K, Marzec KM, Kaczor A, Pilarczyk M, Baranska M. Raman spectroscopy of proteins: a review. J Raman Spectrosc. 2013;44(8):1061-76.

33. Lita A, Kuzmin AN, Pliss A, Baev A, Rzhevskii A, Gilbert MR, et al. Toward Single-Organelle Lipidomics in Live Cells. Anal Chem. 3 sept 2019;91(17):11380-7.

34. Liang W, Sagar S, Ravindran R, Najor RH, Quiles JM, Chi L, et al. Mitochondria are secreted in extracellular vesicles when lysosomal function is impaired. Nat Commun. 18 août 2023;14(1):5031.

35. Almaviva S, Artuso F, Giardina I, Lai A, Pasquo A. Fast Detection of Different Water Contaminants by Raman Spectroscopy and Surface-Enhanced Raman Spectroscopy. Sensors. janv 2022;22(21):8338.

36. Frijhoff J, Winyard PG, Zarkovic N, Davies SS, Stocker R, Cheng D, et al. Clinical Relevance of Biomarkers of Oxidative Stress. Antioxid Redox Signal. 10 nov 2015;23(14):1144-70.

Supplementary Information

Raman spectroscopy of large extracellular vesicles derived from human microvascular endothelial cells to detect benzo[a]pyrene exposure

Geetika Raizada[1], Benjamin Brunel[1*], Joan Guillouzouic[2], Kelly Aubertin[3], Shinsuke Shigeto[4], Yuka Nishigaki[4], Eric Lesniewska[5], Eric Le Ferrec[2], Wilfrid Boireau[1], Céline Elie-Caille[1]

1. Université de Franche-Comté, CNRS, institut FEMTO-ST ; F-25000 Besançon, France
2. Univ Rennes, Inserm, EHESP, Irset (Institut de Recherche en Santé Environnement et Travail), UMR_S 1085, F-35000, Rennes, France
3. Université Paris Cité, MSC, CNRS, IVETh expertise facility, 45, rue des Saints-Pères, 75006 Paris, France
4. Department of Chemistry, Graduate School of Science and Technology, Kwansei Gakuin University, 1 Gakuen Uegahara, Sanda, Hyogo, 669-1330, Japan
5. ICB UMR 6303 CNRS, University of Bourgogne Franche-Comté, F-21078 Dijon, France

*benjamin.brunel@univ-fcomte.fr

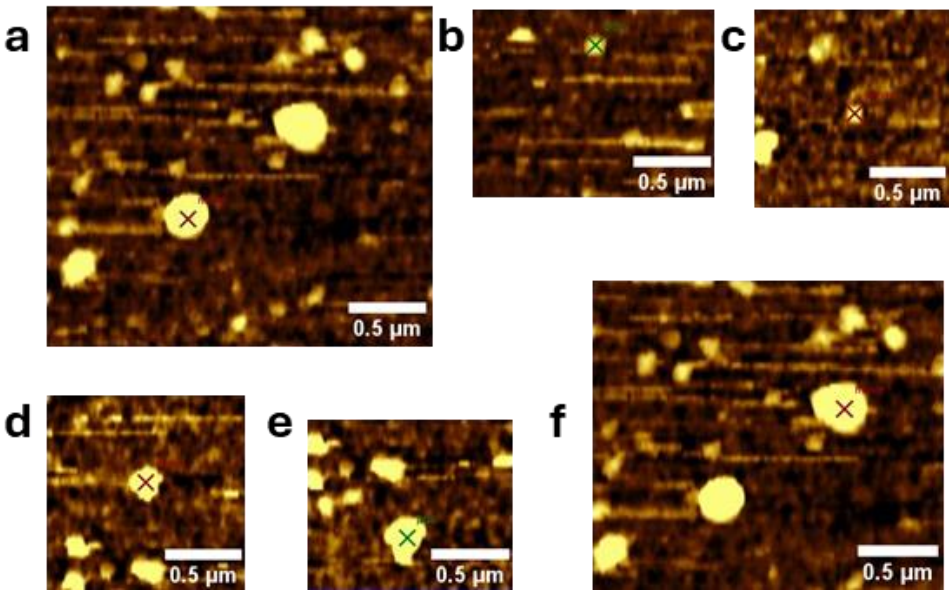

Fig. S1. AFM height images of EVs from control (DMSO) condition. Crosses indicates were TERS measurements were performed.

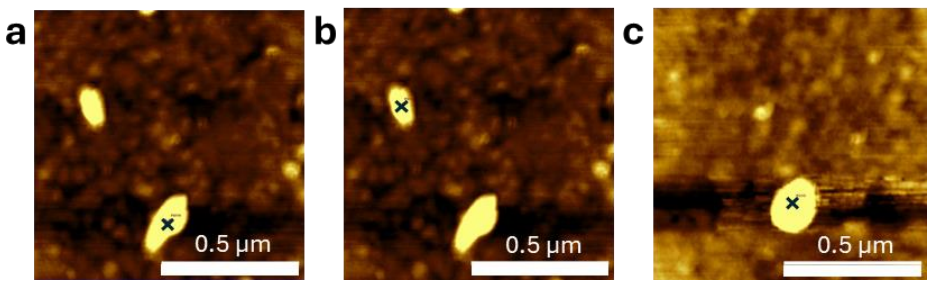

Fig. S2. AFM height images of EVs from treated (B[a]P) condition. Crosses indicates were TERS measurements were performed.

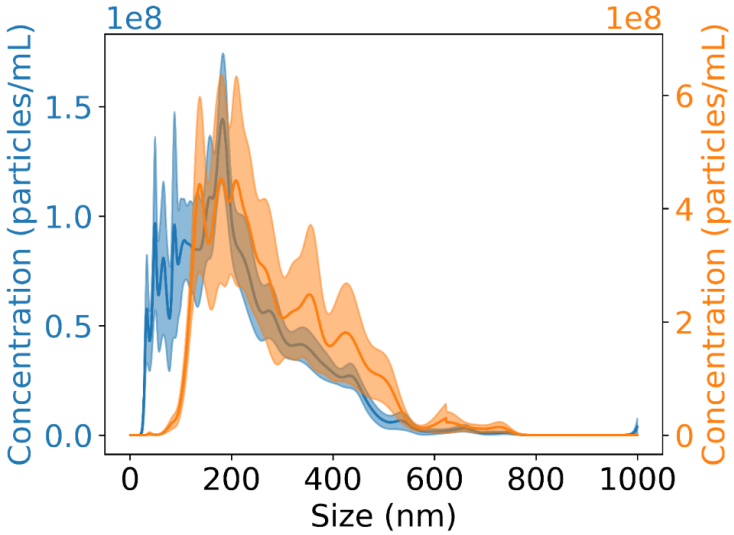

Fig. S3. NTA results showing the concentration of particles as a function of their size for control (blue) and treated (orange) samples. The shaded areas correspond to the standard error of the mean calculated on n = 10 aliquots.